RSC Advances

ROYAL SOCIETY OF CHEMISTRY

www.rsc.org/advances

The photodynamic efficiency of TiO_2 nanotubes against cervical cancer cells (HeLa) driven by near-visible light was successfully tuned by Fe-doping.

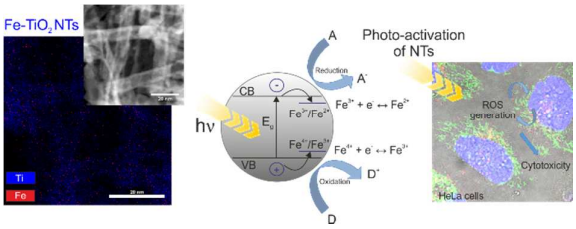

Tuning of photodynamic efficiency of TiO_2 nanotubes against HeLa cancer cells by Fe-doping

Dorota Flak[a*], Emerson Coy[a], Grzegorz Nowaczyk[a], Luis Yate[b], Stefan Jurga[a, c]

[a] *NanoBioMedical Centre, Adam Mickiewicz University in Poznań, Umultowska 85, 61-614 Poznań, Poland*

[b] *CIC biomaGUNE, Paseo Miramón 182, 20009, San Sebastián, Spain*

[c] *Department of Macromolecular Physics, Faculty of Physics, Adam Mickiewicz University in Poznań, Umultowska 85, 61-614 Poznań, Poland*

Abstract

In this study Fe-doped TiO_2 (0.35 to 3.50 wt. % Fe) nanotubes (NTs) were prepared as the potential photosensitizer for the near-visible light driven photodynamic therapy (PDT) against cervical cancer cells (HeLa). Characterization of prepared nanotubes with X-ray diffraction (XRD), Raman spectroscopy and X-ray photoelectron spectroscopy (XPS) confirmed the successful incorporation of Fe^{3+} as a dopant into the TiO_2 matrix, which was mainly composed of anatase phase, while the elemental mapping with the energy dispersive X-ray spectroscopy (EDX) showed homogenous distribution of dopant ions in TiO_2 for both low and high doping level. UV-Vis studies showed that Fe doping in TiO_2 increases the light absorption within the visible range, particularly in case of 0.70 and 1.40 wt. % Fe-TiO_2 and provides additional energy levels within the band gap, that promote the photo-excited charge transport towards conduction band. Photo-cytotoxic activity of prepared Fe-doped TiO_2 NTs was investigated *in vitro* towards cervical cancer cells (HeLa) and compared with human normal fibroblasts (GM07492). Fe-doped TiO_2 NTs exhibited none or lower dark cytotoxicity than un-doped TiO_2 NTs, what confirms their superior biocompatibility. Under the near-visible light irradiation (~405 nm) Fe-doped TiO_2 NTs showed higher photo-cytotoxic efficiency than un-doped TiO_2 NTs, which was found to be dependent on the NTs concentration, but not on the incubation time of cells after the near-visible light irradiation. The highest activity was observed for 0.70 and 1.40 wt. % Fe-TiO_2 NTs. Fluorescent labeling of treated HeLa cells showed distinct morphological changes, particularly in the perimitochondrial area suggesting the mitochondria-

*Corresponding author. E-mail address: flak.dorota@gmail.com or Dorota.Flak@amu.edu.pl

involved apoptosis of cells, but also nuclei and cytoskeleton were subject to the Fe-TiO_2 NTs induced photo-damage. Apoptosis of PDT treated HeLa cells was also confirmed by the use of ethidium homodimer (EthD-1).

Keywords

TiO_2 nanotubes, photodynamic therapy, photo-cytotoxicity, HeLa cells, fibroblasts, cancer treatment, near-visible irradiation

1. Introduction

In recent years photodynamic therapy (PDT) based on inorganic nanomaterials have attracted significant interest due to its advantages over conventional cancer treatments such as surgery, chemotherapy and radiotherapy. These methods often turn to be insufficient, as their results are transient and involve numerous undesirable side effects. PDT among developing treatment methods, is very promising as it uses combination of individually non-toxic components in the presence of molecular oxygen, such as light and photosensitizer (PS) delivered to the target place of diseased tissue.[1] Titanium dioxide (TiO_2), due to its intriguing photocatalytical properties has been proposed as a new photosensitizer in PDT by Fujishima et al.[2] TiO_2 is a well-known and extensively studied material for many applications owing a privileged position due to its properties such as strong light absorption, low dark toxicity and biocompatibility, chemical stability, nature abundance. TiO_2 is widely used not only in areas such as photovoltaics,[3] photocatalysis,[4] but also in biomedicine.[5] Among biomedical applications, next to the photodynamic therapy, TiO_2 is also used in targeted drug delivery, cell imaging, biosensors for biological assay and in genetic engineering.[5]

TiO_2 as a photosensitizer for PDT has been already subject to an intensive research, which proved its photo-cytotoxicity *in vitro* upon UV light exposure towards e.g. cervical cancer cells (HeLa),[6] glioma cells (C6, GMB),[7] bladder cancer cells (T24),[8] leukemic cells (HL60, THP-1),[9] melanoma cells (S-91),[10] colon carcinoma cells (LoVo),[11] breast cancer cells (MCF-7, MDA-MB-468),[12] hepatocellular liver carcinoma cells (HepG2),[13] and *in vivo* e.g. towards cervical cancer cells (HeLa),[14] or bladder cancer cells (T24).[8] The photo-cytotoxic activity of TiO_2 nanomaterials results from its ability to generate electron-hole pairs upon photo-excitation, that in redox reactions can produce reactive oxygen species (ROS). Generated ROS include hydroxyl radicals, hydrogen peroxide, superoxide, and singlet oxygen, which are the cause of cellular death due to the lipid peroxidation in immediate vicinity of a photosensitizer.

Moreover, TiO_2 due to its wide band gap (3.2 eV) exhibits a strong photo-activity only under UV light irradiation, making it an excellent candidate for selective therapy. Therefore, certain modifications of this material leading to the improvement of its photosensitizing properties in the extended spectrum from UV to visible light are still required. In order to improve the efficiency of TiO_2 as a photosensitizer in terms of the increased ROS generation yield, first of all the modification of particles morphology is considered, what is achieved by the use of nanocrystalline material. Use of nanostructures different than nanoparticles may also contribute to the enhanced photosensitizer efficiency, as recently presented by Zhang et al., who developed TiO_2 nanofibers with mixed phases for killing of HeLa cells.[15] These nanofibers exhibited high killing efficiency, which was assigned to the inhibition the recombination of the photo-generated charges, due to stable interface between phases in a single nanofiber. However, such PDT system was highly efficient only under UV light irradiation. The superiority of nanotubular structures has been also proven in case of carbon nanomaterials used for biomedical applications. Functionalized CNTs have shown great potential as sensitizer for PDT,[16] but also as magnetic MRI (Magnetic Resonance Imaging) contrast agent.[17] Therefore, use of nanomaterials with different structures e.g. nanoparticles vs. nanotubes or nanorods may also contribute to the improvement of their efficiency. Another very promising direction of the development of new TiO_2-based photosensitizers is their broadly-understood doping. Doping with foreign metals can be realized e.g. by donor doping (e.g. with W^{6+}, Nb^{5+})[18] or acceptor doping (e.g. Fe^{3+}, Al^{3+}, Cr^{3+})[19] in the cationic sublattice by foreign atoms. This type of modification results in the decrease of the band gap, shifting the light absorption towards the visible region and as well acts as electron/hole traps and therefore alters the photo-excited charges recombination rate.[19] Another important aspect for the improvement of the PDT in cancer treatment with inorganic photosensitizers is to explain the underlying mechanisms behind their photo-cytotoxic activity. Up to date, studied photosensitizers have revealed different level of photodynamic activity that was strongly dependent on the tested biological systems (different cancer cells). Such effect is believed to be related to the changes in the cell signaling and also to different mechanism of cell death after PDT.[20] In case of TiO_2-based photosensitizers, there is still no clear opinion on the PDT mechanism at the subcellular and molecular level. Therefore the imaging of subcellular organelles of cells, that allows for direct observations of therapeutic effects, seems to play an important role.

The main focus of this report is on the effect of Fe-doping on the *in vitro* photo-cytotoxic activity of TiO_2 nanotubes towards cervical cancer cells (HeLa), that are promising new nanostructures for PDT in cancer treatment. So far, considerable efforts has been done to study

the effect of Fe-doping on the photocatalytical properties of TiO_2 nanoparticles, which are directly related to the structural changes, chemical composition, and therefore electronic structure and optical properties of TiO_2 matrix. Briefly speaking Fe-doping extends the absorption threshold of TiO_2 to the near-visible region. While use of the TiO_2 nanoparticles for PDT application has been well reported so far,[21] the use of TiO_2 nanotubes is rare and its activity towards cancer cells is poorly explored, as the main subject of the investigations on these structures reported in the literature concerns only physical aspects of the ROS generation.[22] TiO_2 nanotubes are found to exhibit higher photo-oxidation effect, due to the inhibition the recombination of the photo-generated charges, hence the interest on TiO_2 nanotubes as therapeutic agents for cancer photodynamic therapy. At the beginning we report on the preparation of Fe-doped TiO_2 nanotubes with the nominal composition of 0.35 to 3.50 wt. % Fe in TiO_2, and their physico-chemical characterization with the focus on the required structural and optical properties of an efficient photo-cytotoxic agent for PDT. Further we focus on the *in vitro* photo-cytotoxic activity of prepared nanotubes towards HeLa cell upon near-visible light irradiation as a function of nanotubes composition, concentration and incubation time after PDT treatment. Finally, with *in vitro* cell imaging of HeLa cells we show directly the effect of prepared nanotubes and light irradiation on the morphology of subcellular organelles, what helps to propose the mechanism behind the treatment.

2. Material and methods

2.1. Preparation of nanomaterials

TiO_2 nanomaterials were synthesized using hydrothermally assisted sol-gel technique. Firstly nanoparticles (NPs) were obtained with the sol-gel technique using titanium 3.2 M tetraisopropoxide (TTIP, Sigma Aldrich), which was added dropwise upon N_2 flow to the reaction solution consisted of aqueous 0.1M HNO_3 solution and proper stoichiometric amount of 0.1 M aqueous solution of iron(III) nitrate nonahydrate ($Fe(NO_3)_3 \times 9H_2O$, Sigma Aldrich) and polyethylene glycol (PEG 400, Sigma Aldrich) in molar ratio MR=1 to Ti-precursor upon continuous magnetic stirring in order to obtain required final powder product stoichiometry of 0.35 to 3.50 wt. % Fe in TiO_2. The reaction mixture was then kept under reflux at 80 °C for 4 h until a transparent sol (pale yellow in color) was obtained. The reaction solution was then diluted with deionized water (19 MΩ.cm, v/v=1) and then given to the hydrothermal treatment at 200 °C for 18 h in a Teflon-lined autoclave. Obtained NPs suspension was centrifuged and washed with deionized water. This procedure was repeated three times. The isolated powder was then vacuum-dried (70 °C), calcinated at 400 °C for 2 h and milled in agate mortar to a

fine powder. TiO_2 NTs were obtained using previously prepared NPs. 0.5 g of NPs (0.35 to 3.50 wt. % Fe in TiO_2) was mixed with 50 ml 10 M base solution (NaOH) and given to the hydrothermal treatment in Teflon-lined autoclave at 150 °C for 24 h. The NTs suspension was centrifuged and washed with 0.1 M HCl and deionized water until the suspension reached a pH of 7. Then the powder was dried at 100 °C in air and then calcinated at 400 °C for 2 h.

2.2. Physico-chemical characterization

2.2.1. XRD measurements

The crystal structure and phase composition of prepared nanomaterials were investigated with X-ray diffraction (XRD) using Empyrean (PANalytical) diffractometer with Cu Kα filtered radiation (1.54 Å) and PIXcel 3D detector. The diffractograms were recorded at room temperature using the 2θ angular range of 20 - 80° with a step size of 0.007° by applying continuous scan mode. The phase identification was carried out using the ICCD library data. The crystallite size was calculated using Scherrer's formula from the peak width at half-intensity of the predominant diffraction peak (101).

2.2.2. Raman spectroscopy

Raman spectra of all samples were collected using RENISHAW Raman spectrometer equipped with an optical microscope (Leica 50x objective lens). Red He -Ne laser (633 nm) was used as the excitation source. The Raman spectra were collected over the spectral range of 50 – 1000 cm^{-1}, with 30 s exposition to laser power of 0.85 mW (5 %), in an extended mode, using a holographic grating having 1800 grooves/mm.

2.2.3. Transmission electron microscopy (TEM)

The morphology and chemical composition of the particles were investigated by the transmission electron microscopy (TEM). TEM images were recorded with a high-resolution and analytical HRTEM Jeol ARM 200F operating at 200kV co-equipped with an Energy Dispersive X-Ray Spectrometer (EDX). Prior to the analysis nanoparticles were dispersed in ethanol and drop-wise deposited onto carbon coated copper grids and left to dry under vacuum. The particle size distribution (the average particle size d_{TEM} and standard geometric deviation σ_g) was determined by statistical image analysis using log probability plots. Both the width and the length of NTs were considered.

2.2.4. UV-Vis spectroscopy

The spectral dependence of the transmittance $T(\lambda)$ over the wavelength range λ = 250 - 1000 nm was measured for TiO_2 and Fe-doped TiO_2 sol with UV-Vis spectrophotometer (Perkin Elmer lambda 950). Determination of the position of the absorption edge and band gap energy value (E_g) was based on differential analysis of the transmittance spectra.

2.2.5. X-ray photoelectron spectroscopy (XPS)

XPS experiments were performed in a SPECS Sage HR 100 spectrometer with a non-monochromatic X-ray source (Aluminum Kα line of 1486.6 eV energy and 350 W). The samples were placed perpendicular to the analyzer axis and calibrated using the $3d_{5/2}$ line of Ag with a full width at half maximum (FWHM) of 1.1 eV. An electron flood gun was used to compensate for charging during XPS data acquisition. The selected resolution for the high resolution spectra was 10 eV of Pass Energy and 0.15 eV/step. All Measurements were made in an ultra-high vacuum (UHV) chamber at a pressure below 8×10^{-8} mbar. In the fittings Gaussian-Lorentzian functions were used (after a Shirley background correction), where the FWHM of all the peaks were constrained while the peak positions and areas were set free.

2.3. Biochemical characterization

2.3.1. Cell culture

The human cervical carcinoma cells (HeLa) and human normal fibroblasts (GM07492) were purchased from the European Collection of Cell Cultures and the Coriell Institute for Medical Research, respectively. The cells were cultured as a monolayer on sterile tissue culture plates (Sarstedt) in cell culture medium under standard cell culture conditions at 37 °C, 5% CO_2 in an incubator. Dulbecco's Modified Eagle's Medium (DMEM, Sigma Aldrich) for culture of HeLa cells and Eagle's Minimum Essential Medium (EMEM, Lonza) for culture of fibroblasts, was supplemented with 10 v/v % of FBS (Fetal Bovine Serum, Sigma Aldrich) and 1 v/v % antibiotics (penicillin, streptomycin, Sigma Aldrich) and additionally with 1 v/v % non-essential amino acids (NEAA, Sigma Aldrich) for EMEM. For further biological tests, cells grown to 80% confluence, washed with Hanks' Balanced Salt solution (Sigma Aldrich), then trypsinized, re-suspended in cell culture medium and counted with the Bio-Rad's automated cell counting technique. Then depending on the character of further investigations, the cells were seeded at the necessary density in 96-well plates (for cell viability and cytotoxicity) or

glass bottom dishes (for optical imaging) and grown up to 80% confluence at standard cell culture conditions.

2.3.2. NTs and PDT treatment

Prior to the viability and cytotoxicity assay, sterilized stock suspension of prepared nanotubes (5 mg/ml) in phosphate buffered saline (PBS) with the physiological pH of 7.4 was prepared by sonication. Then the suspension with the final required concentration was prepared by the dilution of the stock solution in cell culture medium and then sonicated before cellular exposure. As-prepared suspensions were added onto previously prepared adherent cells and then co-incubated at 37 °C, 5% CO_2 incubator for the next 24 h before the cell viability tests. Afterwards, prior to the investigation of the photo-cytotoxic activity, as-prepared cells were washed with PBS, then added with PBS as a medium and finally irradiated using near-visible light exposure (2.30 mW/cm^2, ~405 nm) for 40 minutes. The irradiation system was an in-house built lamp with 96 LED diodes emitting light in the near- visible range. After irradiation the medium was exchanged back to cell culture medium and cells were incubated in standard cell culture condition for 3 h or 24 h.

2.3.3. Cell viability – Live/Dead assay

The cell viability, in terms of the metabolic activity, was assessed using the In Cell Analyser apparatus (GE Healthcare). For this purpose two sets of cultured adherent cells in the 96-well plate in the concentration of 0.8×10^4 cells/ml (four wells for each composition and each concentration of NTs), previously co-incubated for 24 h with NTs were prepared. First set was for the experiment with no irradiation and second set for the experiment under light irradiation (40 min). The sets also included negative control (K), and positive control (DMSO), where no NTs and 50 v/v % dimethyl sulfoxide were added, respectively. Further on, prior to the cell viability tests, the cells were washed with PBS. Afterwards, Live/Dead viability Kit (Life Technologies) employing fluorescent dyes, calcein-AM and ethidium homodimer (EthD-1), for staining of live and dead cells was used, respectively. Thus, in live cells the virtually nonfluorescent cell-permeant calcein-AM was enzymatically converted into calcein, producing a measurable green fluorescence (light excitation at 495 nm and emission at 515 nm). In turn EthD-1 enters cells with physical and chemical alterations of cellular membrane and undergoes strong enhancement of bright red fluorescence in dead cells (light excitation at 495 nm and emission at 635 nm). Three individual experiments with four replications for each conditions were carried out intravitally. The images were acquired from 20 fields from each well (objective

Nikon 20x), and then given to the statistical analysis by employing In Cell Developer Toolbox software.

2.3.4. Cytotoxicity and photo-cytotoxicity – WST-1 assay

The cell cytotoxicity (dark conditions) and photo-cytotoxicity (under light irradiation) was also evaluated using WST-1 colorimetric assay (Clontech), based on the reduction of the tetrazolium salt to formazan by cellular dehydrogenases. For this purpose the cells were prepared as described in the previous section (first set for the experiment with no irradiation and second set for the experiment under light irradiation). Cells were then washed with PBS and added with 10 µl of WST-1 reagent solution per well (100 µl) and left for incubation under standard cell culture conditions for 40 min. The generation of the dark yellow colored formazan directly related to the viable cell number was measured at the wavelength of 450 nm. The optical density (OD) was measured using spectrophotometric microplate reader (Anthos Zenyth 340rt). The survival rate of the cells was calculated with the following formula: $\%SR = (OD_{sample}/OD_K) \times 100$.

2.3.5. Optical imaging – confocal microscopy

The confocal fluorescent microscopy was used to study the effect of the PDT treatment (NTs and light irradiation) on the cell morphology and thus their functioning. The fluorescence images were acquired with the scanning confocal microscope (Olympus FV-1000, 60 × S silicone immersion objective).

To assess the morphology of the cells treated with NTs as well as given to the light irradiation, cells were seeded on the glass bottom dishes and grown up to 80% confluence at standard cell culture conditions. Afterwards, the cells were exposed to NTs and light irradiation (as described above). After the incubation the cells were washed with PBS and stained with the green-fluorescent mitochondrial dye and red-fluorescent acidic organelles dye (Mito-Tracker Green FM and Lyso-Tracker Red DND, Life Technologies, respectively), as well as with the green-fluorescent cytoskeleton dye (Oregon green 488 Phallodin, Life Technologies). Finally, the nuclei were stained (Hoechst, Life Technologies). After staining the cells were washed with PBS and added with the Lebovitz supplemented medium without phenol red (Life Technologies).

3. Results and Discussion

3.1. Morphology and structure

Sol-gel synthesis assisted with hydrothermal treatment resulted in white, trough yellowish to light orange nanopowders, along with the increasing Fe content (0.35 to 3.50 wt. % Fe in TiO_2). After the hydrothermal treatment in an alkaline solution TiO_2 nanoparticles transformed into nanotubes as evidenced with the TEM images (Figure 1). Obtained nanotubes consists mainly of anatase crystalline phase as the interplanar distances *d* characteristic for anatase phase were assigned to the lattice planes (101) and (200) (see HRTEM insets in Figure 1a, b and c), what was also confirmed with XRD measurements (Figure 3). The statistical analysis of TEM images allowed for determination of the particle size distribution (right column in Figure 1.). The average length of as prepared nanotubes was below 55 nm and the width below 10 nm (please note given values as insets in particle size distribution graphs in Figure 1). HR-TEM images (insets in Figure 1a, b and c) clearly show that formed nanotubes have a layered, hollow structure and are open-ended. The width of their wall is below 4 nm. The EDX elemental mapping of Fe-doped TiO_2 NTs with the low (0.70 wt. % Fe) and the highest nominal Fe dopant concentration (3.50 wt. % Fe) presented in Figure 2, shows no segregation of Fe indicating the uniform distribution of dopant ions in TiO_2 matrix. Analysis of the EDX spectra showed that the real concentration of Fe in TiO_2 NTs was 0.8 wt. % Fe and 3.35 wt. % Fe, for analyzed samples with the low and highest Fe dopant concentration, respectively. These values of Fe content are close to the stoichiometric ones. Moreover, the EDX analysis shows that no other contamination element was introduced into the Fe-doped TiO_2 NTs during their preparation.
Due to the foreseen application of prepared layered-tubular nanostructures the inner and outer surfaces is one of the advantages in favor of their photo-cytotoxic efficiency.

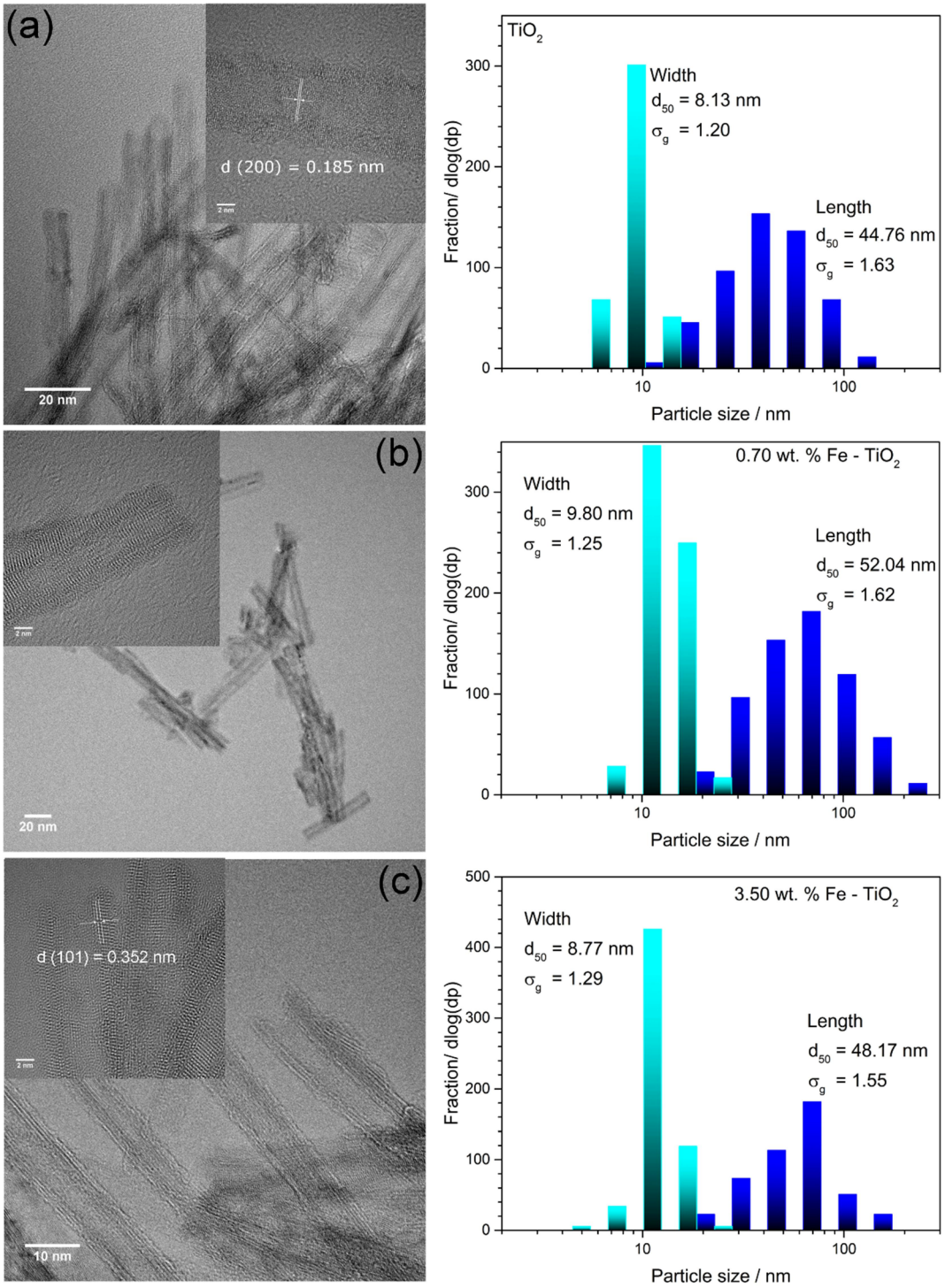

Figure 1. TEM images of prepared TiO_2 NTs (left column) and lognormal size distribution (right column): a) un-doped TiO_2; b) 0.70 wt. % Fe-doped TiO_2 NTs; c) 3.50 wt. % Fe-doped TiO_2 NTs; insets – HRTEM images.

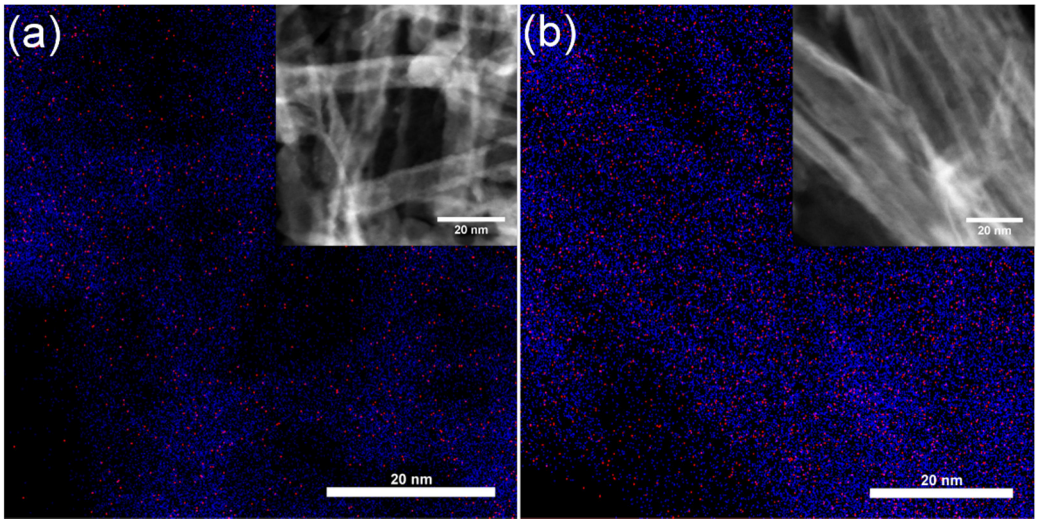

Figure 2. EDX elemental mapping of 0.70 wt. % and 3.50 wt. % Fe-doped TiO_2 NTs; insets - dark field TEM images (blue - titanium Ti, red - iron Fe).

The successful incorporation of Fe^{3+} into TiO_2 matrix was confirmed with XRD and Raman spectroscopy. The X-ray diffractograms of prepared nanoparticles and nanotubes in comparison to commercial TiO_2-P25 nanoparticles (Degussa) are given in Figure 3a and Figure3b, respectively. These patterns match well with the reference diffractograms of anatase, rutile and brookite from ICCD files (PDF#01-082-0514 for anatase, PDF#01-082-0514 for rutile and PDF#00-029-1360 for brookite). Anatase is a dominant phase in all samples. Contribution from rutile phase clearly appears particularly in case of nanoparticles with 2.80 and 3.50 wt. % Fe, as the Bragg reflection assigned to the crystallographic plane (110) at 27.34 ° of rutile is observed.

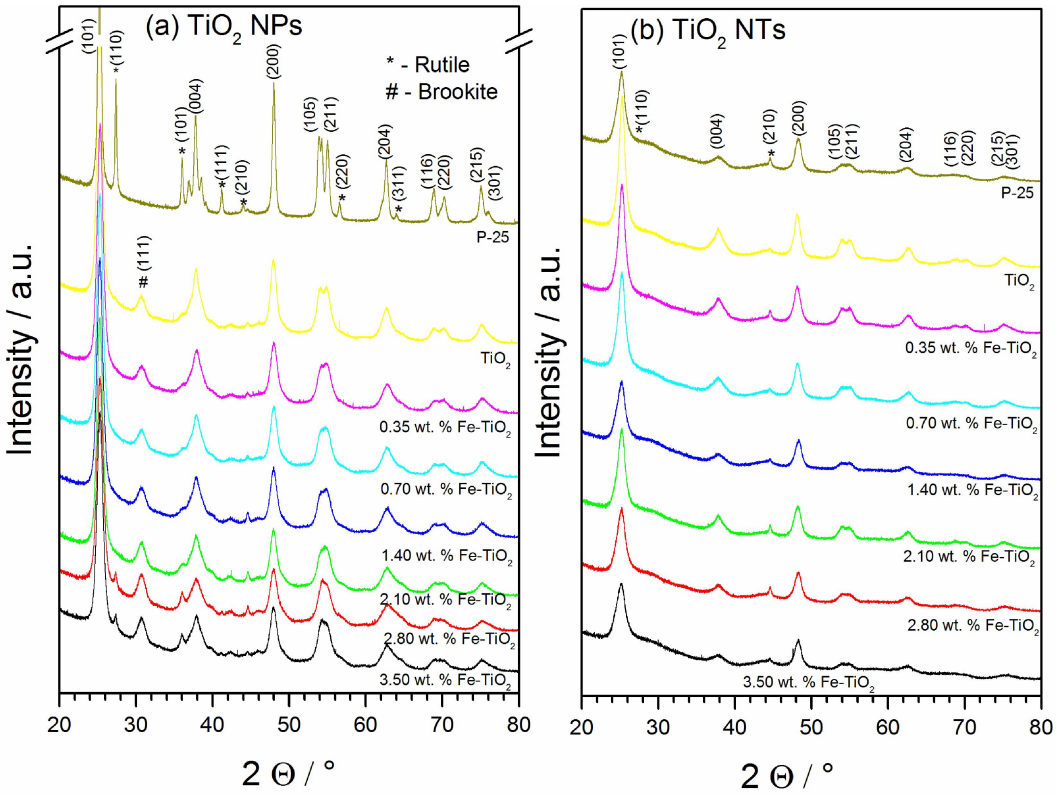

Figure 3. X-ray diffractograms of prepared Fe-doped TiO_2 nanostructures: a) nanoparticles; b) nanotubes.

Comparison of diffractograms of nanoparticles and nanotubes reveals significant differences in the phase composition between these nanostructures. Transition of nanoparticles towards nanotubes resulted in the lowered contribution of the rutile phase and in the disappearance of brookite phase. Such difference in the phase composition is beneficial for photo-catalytical applications of this material as anatase has a wider optical absorption gap and a smaller electron effective mass resulting in a higher mobility of the charge carriers.[23] The distinguishable reflections coming from separated Fe-related phase cannot be found as the diffraction peaks are very broad due to nanosized structures. This is particularly the case of prepared NTs as the reflexes are significantly broadened and of lowered intensity in comparison to NPs. The transition from NPs towards NTs resulted also in the changes of the unit cell volume (Table 1), which is in general higher for NTs. The unit cell volume in case of NPs decreases along with increasing Fe content, whereas in the case of NTs reaches its maximum for 1.40 wt.% and 3.50 wt. % Fe. Taking into account the mismatch between the ionic radii of the host and dopant ions (0.66 Å for Ti^{4+} and 0.55 Å for Fe^{3+}) these results suggest that the incorporation of Fe into TiO_2 matrix likely bears more structural changes in the case of NTs, as it undergoes the structural reorganization under the second hydrothermal treatment in the alkaline solution. In such

scenario of preparation of Fe-doped TiO_2 NTs one has to take into account also the solubility limit of Fe in TiO_2 and its further effect on the properties of doped TiO_2. It was found that level of iron content, but also synthesis parameters such as e.g. used calcination temperature or pH of the TiO_2 containing dispersion, may strongly modify properties of TiO_2, however these are usually non-linear, what results mainly from the solubility limit of dopant ions in host material. The solubility limit of Fe ions in TiO_2 matrix prepared by mechanical alloying was reported to be so far around 1 wt. % Fe in the predominant anatase and admixture of rutile phase.[24] However, when other synthesis route is applied other phase composition can be obtained, and hence the solubility limit may shift even above 20 %, as in case of Fe-doped TiO_2 nanoparticles prepared by the hydrothermal treatment at pH 6.0, which were composed of pure anatase phase.[25] Therefore, in order to provide the highest photocatalytical activity due to the photo-generated charge transfer only to the TiO_2 phase, the optimal level of Fe dopant must be found in correlation to a synthesis method.[26] Moreover, the uniform distribution of Fe ions in the TiO_2 matrix and lack of the formation of separated Fe-related phases must be ensured. Presented results show that our Fe-doped TiO_2 NTs meet these requirements in the whole range of used Fe ion dopant concentration.

Table 1. Summary of data obtained by the X-ray diffraction measurements (lattice parameters and unit cell volume and crystallite size) and by the statistical analysis of the TEM images (particle size distribution) for firstly prepared Fe-doped TiO_2 NPs and the following NTs.

	a(A)		c(A)		c/a Ratio		Volume		d_{XRD} / nm		d_{TEM} / nm (σ_g)	
	NPs	NTs	NPs	NTs	NPs	NTs	NPs	NTs	NPs	NTs	NPs	NTs
TiO_2	3.80	3.79	9.49	9.50	2.50	2.50	136.97	136.88	10.59	8.93	6.80 (1.34)	L 44.26 (1.63) W 8.13 (1.20)
0.35 wt. % Fe - TiO_2	3.80	3.80	9.48	9.50	2.50	2.50	136.67	137.09	9.04	7.44	-	-
0.70 wt. % Fe - TiO_2	3.79	3.80	9.49	9.51	2.50	2.50	136.75	137.26	9.20	6.86	11.45 (1.33)	L 52.04 (1.62) W 9.80 (1.25)
1.40 wt. % Fe - TiO_2	3.79	3.81	9.49	9.49	2.50	2.49	136.36	138.03	9.45	7.02	-	-
2.10 wt. % Fe - TiO_2	3.79	3.81	9.50	9.50	2.51	2.50	136.47	137.65	9.07	7.85	-	-
2.80 wt. % Fe - TiO_2	3.79	3.81	9.50	9.50	2.51	2.49	136.17	137.97	8.84	6.96	-	-
3.50 wt. % Fe - TiO_2	3.79	3.82	9.49	9.49	2.51	2.48	136.12	138.42	9.29	6.04	9.46 (1.31)	L 48.17 (1.55) W 8.77 (1.29)

Raman spectroscopy confirmed the XRD results on the structure and phase composition of prepared Fe-doped TiO_2 nanostructures. The presence of characteristic bands for the predominant phase of anatase and contribution of rutile and brookite phase for TiO_2 NPs have been found (Figure 4). Raman bands of anatase are observed at 635 cm^{-1}, 514 cm^{-1}, 396 cm^{-1}, 197 cm^{-1} and very sharp characteristic band at 144 cm^{-1}.[27] Respectively, for rutile, the following bands can be seen: at 610 cm^{-1}, 446 cm^{-1} and 240 cm^{-1}.[28] In addition, trace contribution of the

brookite phase increasing along with Fe dopant amount, is observed as a weak bands at: 247 cm^{-1}, 362 cm^{-1}, 454 cm^{-1} and 588 cm^{-1}.[27] Moreover, upon increasing Fe-doping the distortion of the TiO_6^{8-} octahedral is observed in NPs as the broadening and slight shift of the bands between 380 cm^{-1} and 720 cm^{-1}, which are assigned to O-O interactions. Transformation of NPs towards NTs resulted in the definite phase change as a disappearance of brookite trace contribution and a doublet formation within the 320-220 cm^{-1} range have been observed for NTs, which is corresponded to the increase in the binding energy of both Ti $2p_{3/2}$ and O 1s bands, what suggests the strengthening of Ti-O bonds, when the nanostructure alters from NPs to NTs. No characteristic peaks corresponding to Fe containing phase have been found, however a small shift of Raman bands towards higher frequency have been observed for Fe doped samples.

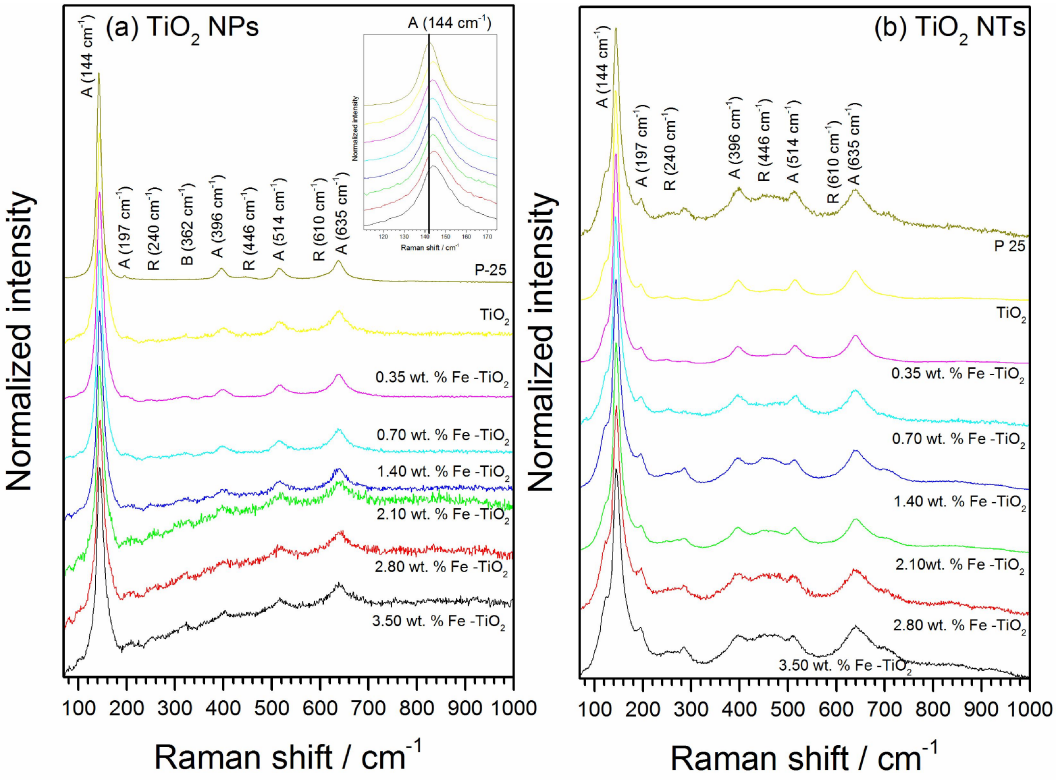

Figure 4. Raman spectra of prepared Fe-doped TiO_2 nanostructures: a) nanoparticles; b) nanotubes.

These results, show that the controlled substitutional doping and homogenous distribution of Fe^{3+} in the TiO_2 matrix consisting mainly of anatase phase were achieved. These are the main factors determining the photocatalytical properties and hence the photo-cytotoxic activity of obtained nanostructures, what is related to an efficient reduction of the photosensitizer band gap upon Fe doping.

3.2. Optical properties

The UV-Vis study showed an increasing absorbance along with the increasing content of Fe in TiO_2. In addition, the band gap edge is slightly shifted to a longer wavelength, with the maximum for 0.70 and 1.40 wt. % Fe-TiO_2. Differential analysis of the UV-Vis spectra (d/dx) as a function of the energy and wavelength (Figure 5) revealed inflections of the spectra, suggesting the contribution of more than one transition energy for Fe-doped TiO_2. Firstly, the dominating peak at around 385 nm (3.22 eV) exhibits tailing towards lower energy, what suggest the increased density of states in the forbidden band, that is related to the contribution of different polymorphic phases of TiO_2 that were found with the XRD measurements. Secondly, next to the dominating peak additional transition energy levels at the lower energy at around 416 nm (2.98 eV) are present in case of Fe-doped TiO_2 and are developing along with the increasing content of Fe. These might be associated with the Fe-impurity related donor energy levels near the valence band of TiO_2. Similar results were reported for rutile phase of TiO_2 doped with Fe ions within its solubility limit, which was reported to be 1 wt. % Fe in rutile.[25] However, when considering the position of the band gap energy no significant shift has been observed for the samples, with the exception of 0.35 wt. Fe-TiO_2, which is slightly shifted towards longer wavelengths. In summary, Fe doping leads to the increased light absorption within the visible range (above 400 nm) and provides additional energy levels on the lower energy side that may in turn significantly promote the photo-excited charge transport towards conduction band in the prepared Fe-doped TiO_2 nanostructures.

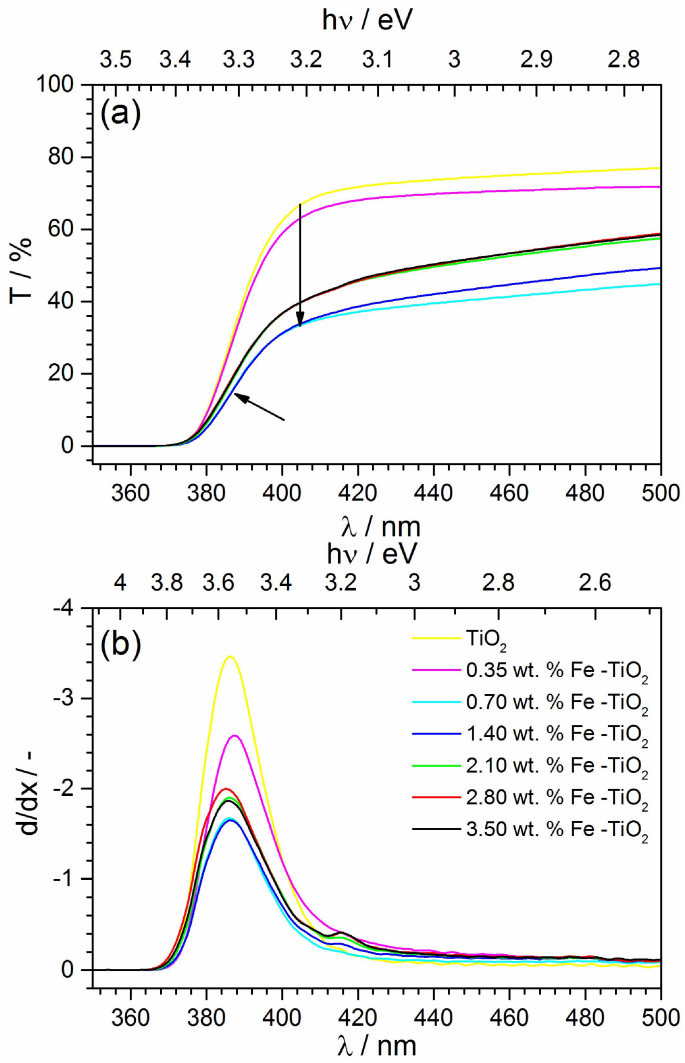

Figure 5. UV-Vis analysis: a) transmittance spectra of Fe-doped TiO_2; b) differential analysis of the UV-Vis spectra (d/dx) as a function of the energy (top axis) and wavelength (bottom axis). The legend in graph b refers to both graphs.

3.3. Chemical composition and electronic structure

In order to determine whether the Fe-doping into the TiO_2 matrix was achieved the XPS investigation were performed on the TiO_2 and 0.70 wt. % Fe-TiO_2. O 1s spectra (Figure 6a) show one component associated to Ti-O bonds at around 530.1 eV and other two minor components at higher binding energy at around 531.7 and 533.4 eV. Such shouldering may be associated to C=O and C-O bonds, respectively, that are an evidence for the unavoidable carbon contaminants.[29] Ti 2p spectra presented in Figure 6b show distinct single peak at around 458.8 eV, which correspond to Ti^{4+} species assigned to Ti-O bonds. The spectra also show the Shake-up peaks between 468 and 480 eV, characteristic of TiO_2 material.[30] The recorded Fe 2p spectra (Figure 6c), although presenting low intensity, confirm the presence of iron in the samples as

the characteristic peak corresponding to Fe $2p_{3/2}$ core level is located around 710 eV near the position of Fe^{3+} species assigned to Fe-O bonds.[31] The total content of iron calculated from the areas of the photoelectron peaks showed a concentration of around 0.3 at.% (0.62 wt.%) for sample 0.70 wt. % Fe. These results are consistent with X-ray diffraction, confirming the successful doping.

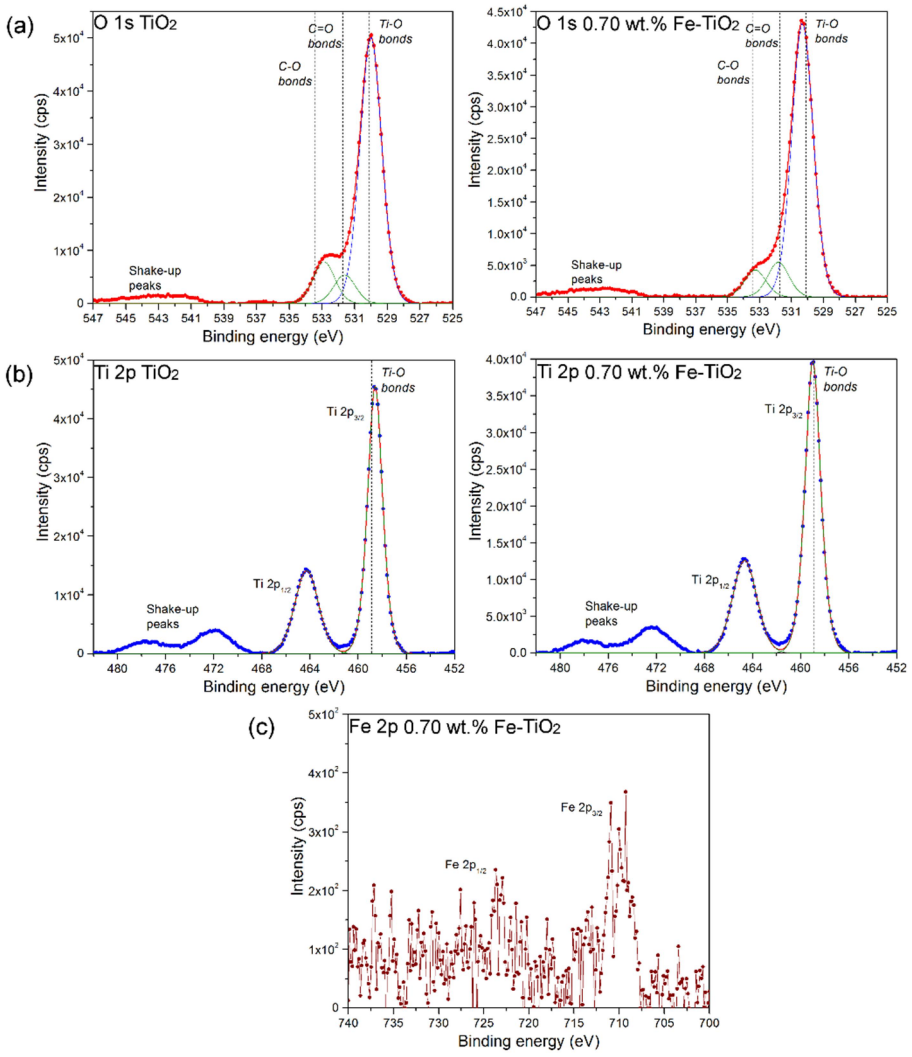

Figure 6. XPS spectra of TiO_2 and 0.70 wt. % Fe-TiO_2 NTs: a) O 1s core level; b) Ti 2p core level; c) Fe 2p core level.

3.4. Photo-cytotoxic activity *in vitro*

Photo-cytotoxic activity of Fe-doped TiO_2 NTs was investigated towards cervical cancer cells (HeLa) and compared to human normal fibroblasts (GM07492). For this purpose the Live/Dead viability assay employing fluorescent dyes, calcein-AM and ethidium homodimer (EthD-1) was used. Figure 7 shows the photo-cytotoxic activity of prepared TiO_2 NTs as a function of NTs concentration of 0, 50, 100, 200 and 500 µg/ml for un-doped TiO_2 and 0.70 wt. % Fe-TiO_2 NTs.

The photo-cytotoxic activity of prepared NTs was also investigated as a function of NTs composition (0 - 3.50 wt. % Fe-TiO_2) and as a function of incubation time after PDT treatment (3h and 24 h) prior to the further investigations, what is presented in Figure 8. Viable cell fraction (of Hela and fibroblasts) in case of non-irradiated cells in general decreases along with the increasing NTs concentration, both in case of un-doped TiO_2 and 0.70 wt. % Fe-doped TiO_2 NTs. However, Fe-doped TiO_2 NTs exhibit none or lower dark cytotoxicity then un-doped TiO_2 NTs, what confirms their biocompatibility in the absence of light irradiation. Upon the near-visible irradiation the significant decrease of the viable cell fraction is observed and again Fe-doped TiO_2 NTs exhibit higher photo-cytotoxic activity the un-doped TiO_2 NTs. In case of HeLa cells it appears that lower concentration of NTs is more suitable for photosensitizing, as in case of 500 μg/ml no significant decrease of the viable cell fraction is observed upon irradiation. Therefore, for further investigations an intermediate concentration of 100 μg/ml of NTs was chosen. When considering the composition of TiO_2 NTs the data demonstrated in Figure 8 shows that the photo-cytotoxic activity of Fe-doped TiO_2 NTs depends non-linearly on the Fe^{3+} dopant ion content. The highest activity was observed for TiO_2 NTs doped with 0.70 and 1.40 wt. % Fe^{3+}. In turn, the comparison of their photo-cytotoxic activity at different incubation time of cells after near-visible light irradiation (3h and 24h) reveals no significant effect on the decrease of the HeLa cell viability. This testifies for the Fe-doped TiO_2 NTs immediate photo-cytotoxic action in the HeLa cell environment, since the generated ROS have a short life-time. However, in case of fibroblasts, longer incubation time after light irradiation, particularly in cells treated with TiO_2 NTs with higher Fe-dopant concentration, results in significantly lower photo-cytotoxic activity. This suggest that normal fibroblasts are able, over longer time after PDT treatment, withstand its toxic effects, as they may further proliferate. It is known, that ROS generated during light irradiation may cause cellular damage, but also, depending on the treatment conditions, may lead to either cellular repair of cells or apoptotic cell death or necrosis.[32] These results are confirmed with the fluorescent images presented in Figure 9, showing the photo-cytotoxic activity of Fe-doped NTs in different concentrations (representative images for TiO_2 and 0.70 wt. % Fe-TiO_2 NTs at concentration of 100 and 500 μg/ml). There upon NTs and PDT treatment with the near-visible light irradiation (bottom row) a considerable contribution of dead cells, indicated by the red fluorescence, is observed. As the use of calcein-AM in association with ethidium homodimer (EthD-1) allows the evaluation of cell apoptosis through the detection of esterase activity and cellular membrane physical and chemical alterations,[33] it may be proposed that upon Fe-doped TiO_2 NTs and light irradiation HeLa cells undergo an apoptosis.

The effect of the Fe-doping on the photo-cytotoxic activity of TiO_2 nanostructures has been previously investigated by George et al.[34] However, these were TiO_2 NPs applied for the inactivation of macrophage cell line RAW 264.7. They found that the photo-cytotoxic activity during similar as in our case near-visible irradiation is incremental with increasing content of Fe^{3+} ion content (0 – 10 wt. % Fe). This is in contrast with our results on Fe-doped TiO_2 NTs, as we observed non-linear behavior of the photo-cytotoxic activity vs. Fe-dopant content, with the maximum activity for 0.70 and 1.40 wt.% Fe-TiO_2 NTs. The same behavior we observed in case of optical properties of prepared nanostructures, where these two samples exhibited the highest absorption above 400 nm (Figure 5). Moreover, it has to be taken into account that Fe-doping in case of TiO_2 NTs formation leads to a change of the phase composition (Figure 3), as well as the surface atomic rearrangements and coordination, resulting in different photo-cytotoxic activity. Finally, these results cannot be directly compared as the investigated nanostructures and biological system in our experiments was different. However, these two reports unequivocally confirm, that Fe-doping leads to the improvement of the *in vitro* photo-cytotoxic activity of TiO_2 nanostructures.

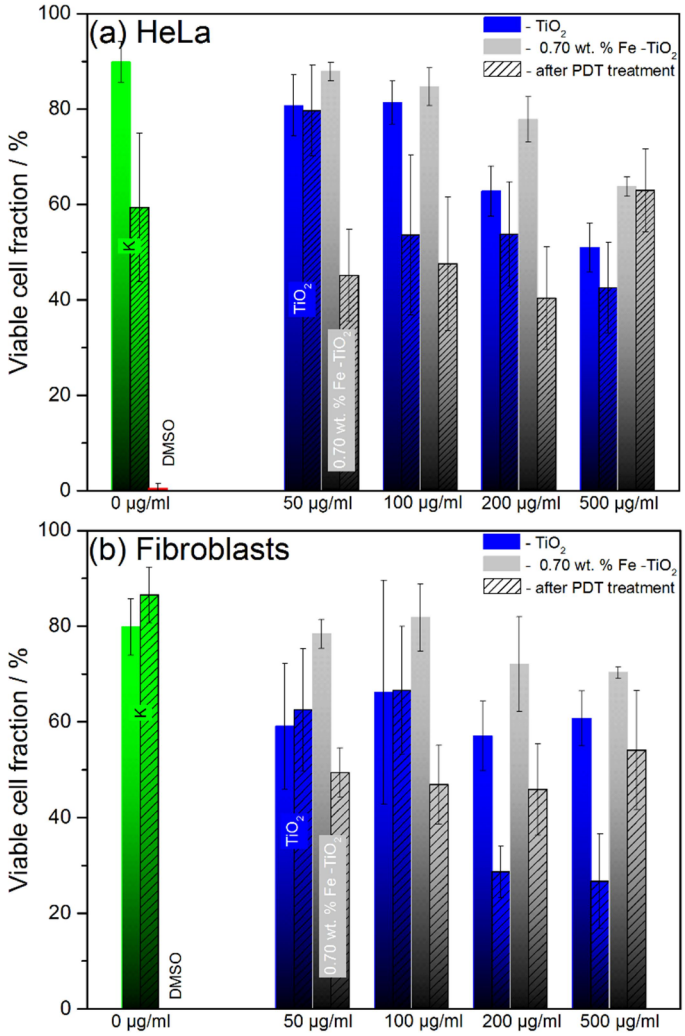

Figure 7. Photo-cytotoxic activity of TiO_2 and 0. 70 wt. % Fe-TiO_2 NTs towards: a) HeLa and b) fibroblasts, as a function of NTs concentration (0, 50, 100, 200, 500 µg/ml); (K – negative control i.e. cells non-treated with NTs, DMSO – positive control i.e. cells treated with DMSO, PDT treatment – exposure to NTs and near-visible light irradiation, ~405 nm).

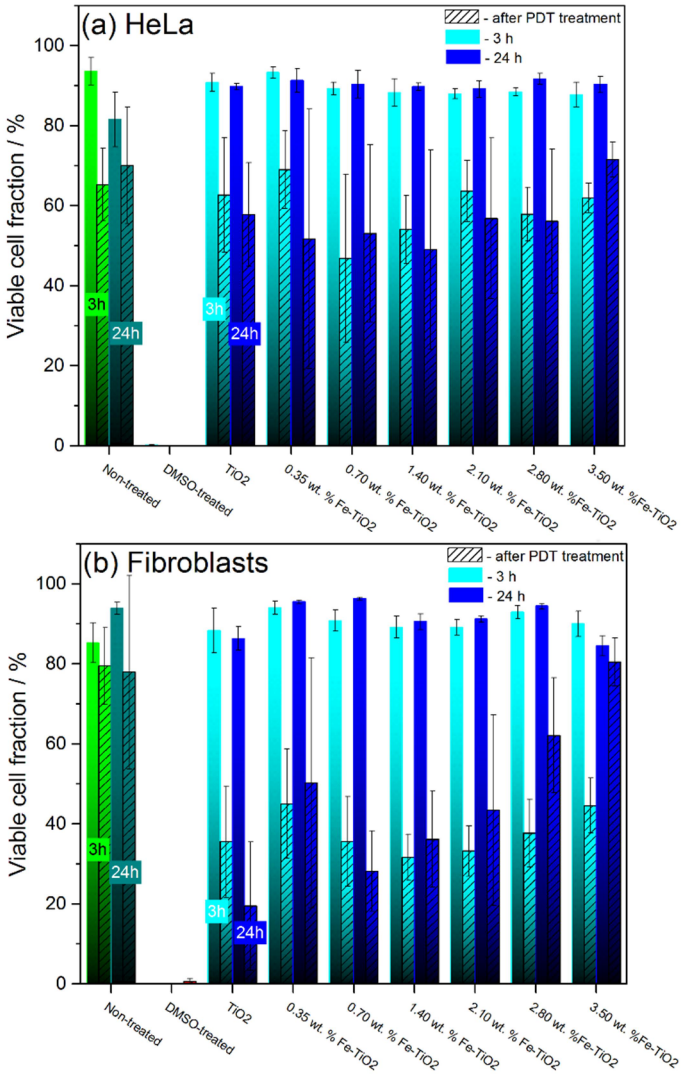

Figure 8. Photo-cytotoxic activity of Fe-doped TiO_2 NTs towards HeLa cells and fibroblasts as a function of NTs composition (0 – 3.50 wt. % Fe) and time of incubation after PDT treatment (3h and 24 h).

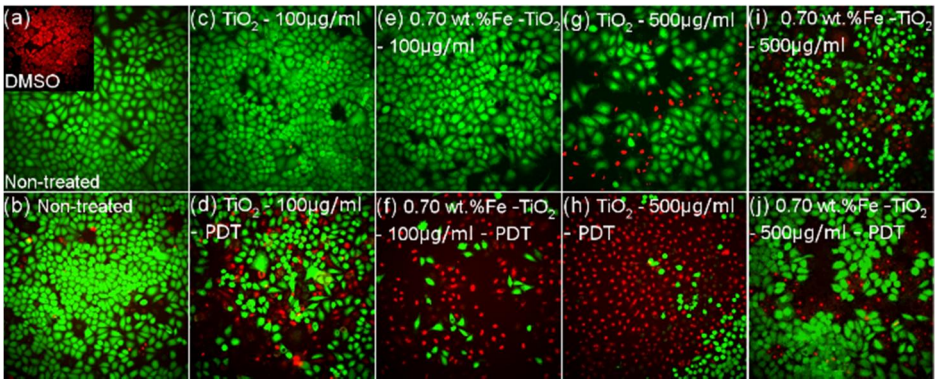

Figure 9. Fluorescent images showing photo-cytotoxic activity of Fe-doped TiO_2 NTs in different concentrations (representative images for TiO_2 and 0.70 wt. % Fe-TiO_2 NTs at concentration of 100 and 500 µg/ml) towards HeLa cells determined with Live/Dead fluorescent assay (by calcein-AM and EthD-1 fluorescence staining) with the use of the In Cell Analyser apparatus. Cells with green fluorescence are considered as viable cells, whereas those with red fluorescence are considered as dead cells. Upper panel - non-irradiated cells, lower panel -irradiated cells (near-visible light irradiation, ~405 nm). Please see the description of treatment conditions in the images.

For further investigations of photo-cytotoxic activity of prepared NTs towards HeLa cells the WST-1 assay was used. Obtained results of survival rate (SR%) of cells exposed to TiO_2 and 0.70 wt.% Fe-TiO_2 NTs as a function of their concentration are presented in Figure 10. These values of the SR% of HeLa cells upon NTs exposure and PDT treatment are controversial in comparison to the results presented above. The WST-1 assay appeared to overestimate the SR% at all tested concentrations. Moreover, the SR% increases along with the increasing concentration of NTs and PDT treatment, particularly in case of TiO_2 NTs. However in case of 0.70 wt.% Fe -TiO_2 NTs the small decrease of the SR% is observed upon PDT treatment. These results suggest that WST-1 assay failed to detect a decrease of SR% of HeLa cells in relative comparison to the previously used Live/Dead viability assay in the presence of Fe-doped TiO_2 NTs. The available reports on the photo-cytotoxicity of photoactive nanomaterials confirm presented here results. It was evidenced that tetrazolium dyes such as WST or MTT used for viability and proliferation tests, particularly in case of cells exposed to ROS generating nanomaterials and upon light irradiation, can undergo the non-cellular reduction, as the O_2^- level in such environment is strongly disturbed in comparison to the not perturbed cells.[35]

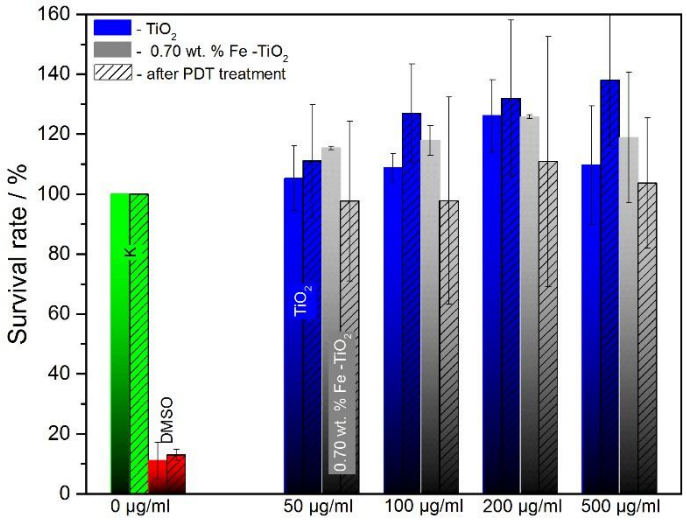

Figure 10. Dose-dependent HeLa cells survival rate after exposure to TiO_2 and 0.70 wt. % Fe-TiO_2 NTs and PDT treatment (near visible light irradiation, ~405 nm) for 24 h determined by WST-1 assay. The survival rate values were expressed as a percent of the read value in negative control wells (K).

3.5. Cell morphology

The cell morphology images with confocal focus of HeLa cells given to NTs and near-visible light irradiation (~ 405 nm) are presented in Figure 11 and Figure 12. In order to determine the effect of NTs and PDT treatment on the HeLa cells morphology two different approaches of staining of cells were taken. The first one was the observation of the NTs and PDT treatment effect on the subcellular organelles such as mitochondria, lysosomes and nuclei, what was achieved by the staining green of mitochondria, staining red of lysosomes and staining blue of nuclei (Figure 11). The second approach was to observe the effect of the NTs and PDT treatment on the cytoskeleton of HeLa cells, where the staining green of cytoskeleton and staining blue of nuclei was used (Figure 12).

Confocal images in Figure 11 show the effect of the NTs composition (TiO_2, 0.70 wt.% Fe-TiO_2 and 3.50 wt.% Fe-TiO_2 NTs), of the PDT treatment with near-visible light irradiation (40 min), as well as of the time of incubation after irradiation (PDT 3h and PDT 24 h) prior to cell viability investigation. In all applied PDT treatment conditions, the control samples, i.e. HeLa cells non-treated with TiO_2 NTs, were also investigated, and their images are given in the first column (Figure 11a, b, c). The cell morphology of control cells is largely unchanged, which is also the case of non-irradiated cells only treated with NTs as stained subcellular organelles do not show any significant changes. These observations confirm the investigated cytotoxicity and photo-cytotoxicity activity of prepared Fe-doped TiO_2 NTs elaborated with the Live/Dead.

However, the cells given to the PDT treatment with the near-visible light irradiation exhibit photochemical injuries, which are observed particularly in case of cells exposed to 0.70 wt. % Fe-TiO_2 NTs, as the mitochondria do not show no longer highly filamentous and well-spread through the cell structure, but take more granular form, particularly in the perinuclear region. Similarly, upon PDT treatment the nuclei of HeLa cells show visible morphological alterations, mainly definite shape changes and fragmentation, also indicating their photochemical damage. When observing lysosomes, they are also affected by the NTs and PDT treatment, as no significant red fluorescence related to their presence was no longer clearly visible, when compared to the non-irradiated cells. Similar effects of Fe-doped TiO_2 NTs and PDT treatment on the subcellular organelles are observed for both cases of 3h and 24 h of cells incubation after irradiation prior to the further investigations.

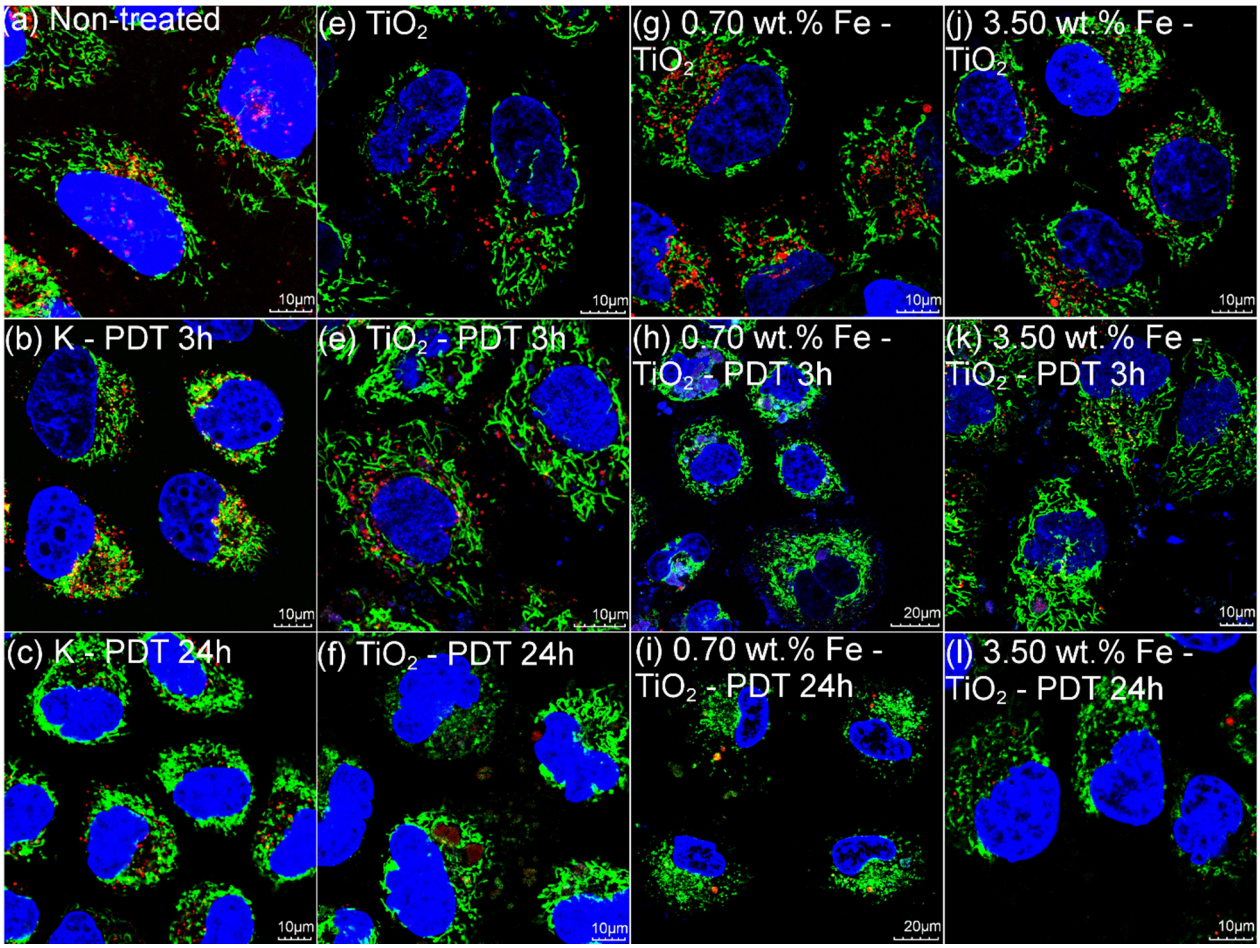

Figure 11. Morphology of HeLa cells co-incubated with TiO_2, 0.70 wt. % Fe-TiO_2 and 3.50 wt. % Fe-TiO_2 NTs (top row), as well as given to 3h (middle row) and 24h (bottom row) of incubation after PDT treatment (near-visible light irradiation, ~405 nm) observed with confocal microscopy. The cell's organelles were stained as follow: green mitochondria (Mito-Tracker), red lysosomes (Lyso-Tracker) and blue nuclei (Hoechst).

The effect of the NTs and PDT treatment on the morphology of HeLa cells with particular focus on the cytoskeleton structure is presented in the Figure 12. Upon NTs exposure in dark conditions (upper row) no significant morphology and cytoskeleton changes can be found, however the F-actin building the cytoskeleton seems to be slightly affected in case un-doped TiO_2 NTs. In turn the PDT treatment with the near-visible light irradiation induced a disorganization and reduction in the number of actin filaments in cells exposed to NTs, more specifically in the case of the intermediate filaments. The long filaments tend to fold and clump into more granular structure than fibrous one. Additionally, as particularly presented in Figure 12 d, these changes seems to begin and spread from the perimitochondrial area. Therefore, these alterations upon PDT treatment in disposition of cytoskeleton, more specifically the intermediate filaments, could be induced by the alterations in the mitochondria, through the oxygen species generated after exposure to light, as the significant morphological changes of the mitochondria were likewise observed. Similar observation and findings were also reported by Robertson et al.[20]

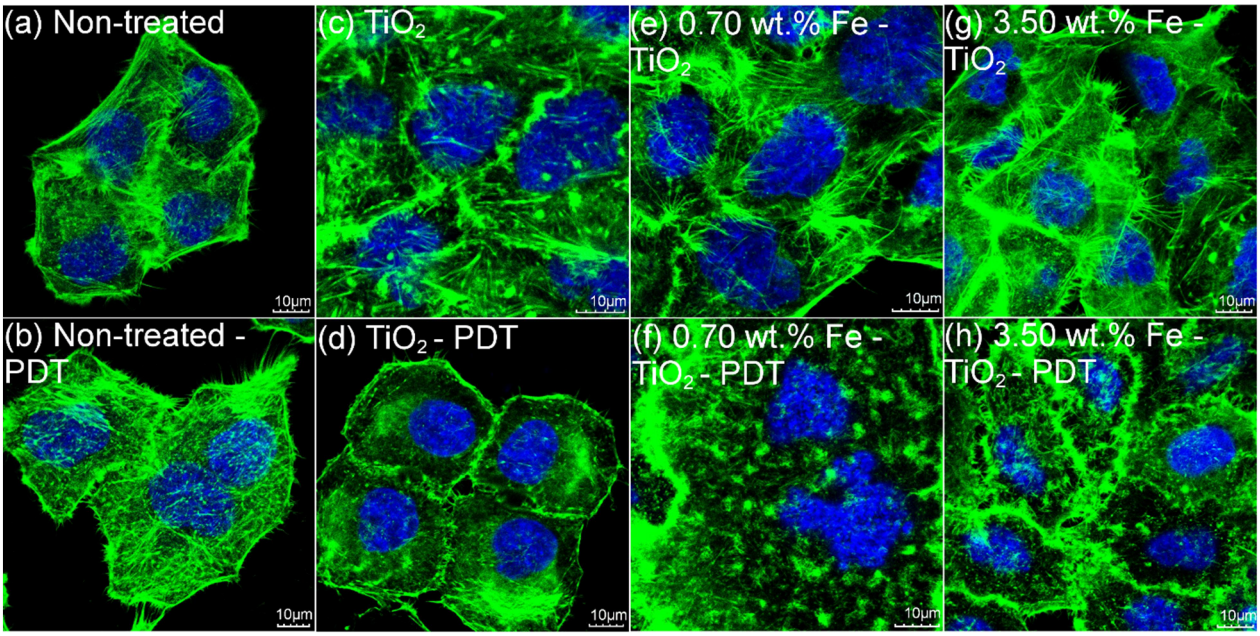

Figure 12. The morphology and cytoskeleton of HeLa cells co-incubated with TiO_2, 0.70 wt. % Fe-TiO_2 and 3.50 wt. % Fe-TiO_2 NTs, as well as given to the PDT treatment (near-visible light irradiation, ~405 nm). The cell's nuclei and cytoskeleton were stained green and blue with Oregon Green 488 phallodin and Hoechst, respectively.

To summarize, the PDT treatment with the use of Fe-doped TiO_2 NTs and near-visible light irradiation resulted in the clearly visible morphological mitochondrial changes. This suggests that these light-activated nanostructures may directly interact with the mitochondria causing

their dysfunction, which in turn may indirectly cause the dysfunction of other cellular structures, e.g. cytoskeleton, as it was presented. These findings indicate the mitochondria-involved apoptosis of cells induced by Fe-doped TiO_2 NTs exposure and light irradiation. However, not only mitochondria, but also other subcellular organelles are subject to the photochemical damage upon NTs. Observed nuclei fragmentation and loss of nuclear DNA content indicates that cells upon PDT treatment turn into apoptotic cells, as it was also observed in case of fluorescence imaging of HeLa cells stained with the EthD-1 in Figure 9. Moreover, NTs may bind to the lysosomal membrane causing its rapture upon irradiation, what also contributes to the killing effect of the cancer cells,[36] however this must be further investigated. It should be also noted that the cellular up-take of nanostructures such as e.g. nanotubes may not be always an ultimate requirement for photo-toxic activity. Our observations are in accordance with results presented by George et al. for Fe-doped TiO_2 nanoparticles.[34] Therefore, nanostructures associated also with the outer side of the cell membrane or in close vicinity may also contribute to the photo-cytotoxic activity, however in different manner depending on the type of generated ROS.

Conclusions

In conclusion, the un-doped and Fe-doped TiO_2 (0.35 to 3.50 wt. % Fe) NTs were successfully prepared by the hydrothermal treatment in an alkaline solution of previously synthesized NPs by hydrothermally assisted sol-gel method. The successful substitutional incorporation of Fe^{3+} into TiO_2 matrix was confirmed with the XRD, Raman spectroscopy and XPS. In addition, EDX elemental mapping showed no segregation of Fe indicating the uniform distribution of dopant ions in TiO_2 matrix both for low and high doping level. UV-Vis studies proved that Fe doping in TiO_2 increases the light absorption within the visible range, particularly in case of 0.70 and 1.40 wt. % Fe-TiO_2 and provides additional energy levels within the band gap that promote the photo-excited charge transport towards conduction band. Photo-cytotoxic activity of prepared Fe-doped TiO_2 NTs was investigated towards cervical cancer cells (HeLa) in comparison to human normal fibroblasts (GM07492). Fe-doped TiO_2 NTs exhibited none or lower cytotoxicity than un-doped TiO_2 NTs in the absence of light irradiation, what confirms their superior biocompatibility and potential application of these nanostructures in the biomedicine field. The viable cell fraction in the absence of light irradiation in general was decreasing along with the increasing NTs concentration, both in case of un-doped $TiO_2$and Fe-doped TiO_2. Upon the near-visible irradiation the significant decrease of the viable cell fraction was observed particularly for Fe-doped TiO_2. The investigation on the effect of the

NTs concentration on their photo-cytotoxic activity showed that lower concentration is more suitable for photosensitizing, as in case of 500 μg/ml no significant decrease of the viable cell fraction was observed. The photo-cytotoxic activity of Fe-doped TiO_2 NTs depends non-linearly on the Fe^{3+} dopant ion content. The highest activity was observed for 0.70 and 1.40 wt. % Fe-TiO_2 NTs. No significant effect of the incubation time of cells after near-visible light irradiation (3h and 24h) on the photo-cytotoxic activity of Fe-doped TiO_2 NTs was observed in case of HeLa cells. However, in case of fibroblasts, longer incubation time after light irradiation, particularly in cells treated with TiO_2 NTs with higher Fe^{3+} ion dopant concentration, resulted in significantly lower photo-cytotoxic activity. When HeLa cells were exposed to Fe-doped TiO_2 NTs and near-visible light irradiation and apoptosis was detected by the use of ethidium homodimer (EthD-1).Moreover, HeLa cells exposed to NTs and light irradiation showed clearly visible morphological changes, particularly in the perimitochondrial area indicating the mitochondria-involved apoptosis of cells. However, also nuclei and cytoskeleton were subject to the Fe-TiO_2NTs induced photo-damage. This research highlights, that presence of Fe dopant in TiO_2NTs provides an excellent photo-sensitizing properties, as it may reduce the recombination of the photo-generated charges and therefore more ROS can be produced in the cell vicinity to induce their dead upon light irradiation. As it was presented both in the physico-chemical and biological characterization, the strongest effect was observed particularly for 0.70 and 1.40 wt. % Fe-doped TiO_2 NTs. As future aspects of PDT systems based on Fe-doped TiO_2 NTs, the improvement of their higher specificity towards HeLa and/or other cancer cells must be considered.

Acknowledgements

This work has been financially supported by the National Centre for Research and Development under research grant “Nanomaterials and their application to biomedicine”, contract number PBS1/A9/13/2012, as well as the International PhD Projects Programme of Foundation for Polish Science operated within the Innovative Economy Operational Programme (IE OP) 2007-2013 within the European Regional Development Fund.

References

1 J. U. Menon, P. Jadeja, P. Tamble, K. Vu, B. Yuan and K. T. Nguyen, *Theranostics*, 2013, **3**, 152-166.
2 A. Fujishima, J. Ootsuki, T. Yamashita and S. Hayakawa, *Photomed. Photobiol.*, 1986, **8**, 45-46.

3 I. Iatsunskyi, M. Pavlenko, R. Viter, M. Jancelewicz, G. Nowaczyk, I. Baleviciute, K. Załęski, S. Jurga, A. Ramanavicius and V. Smyntyna, *J. Phys. Chem. C*, 2015, **119**, 7164-7171.

4 A. Cybula, G. Nowaczyk, M. Jarek and A. Zaleska, *J. Nanomater.,* 2014, **2014**, 1-9.

5 Z. Fei Yin, L. Wu, H. Gui Yang and Y. Hua Su, *Phys. Chem. Chem. Phys.*, 2013, 15, 4844-4858.

6 Z. Li, X. Pan, T. Wang, P.-N. Wang, J.-Y. Chen and L. Mi, *Nanoscale Res. Lett.,* 2013, **8**, 96.

7 S. Yamaguchi, H. Kobayashi, T. Narita, K. Kanehira, S. Sonezaki, Y. Kubota, S. Terasaka and Y. Iwasaki, *Photochem. Photobiol.*, 2010, **86**, 964-971.

8 Y. Kubota, T. Shuin, C. Kawasaki, M. Hosaka, H. Kitamura, R. Cai, H. Sakai, K. Hashimoto and A. Fujishima, *British Journal of Cancer*, 1994, **70**, 1107-1111.

9 K. Huang, L. Chen, M. Liao and J. Xiong, *Int. J. Photoenergy*, 2012, **2012**, 1-8.

10 A. Jańczyk, A. Wolnicka-Głubisz, K. Urbanska, H. Kisch, G. Stochel and W. Macyk, *Free Radic. Biol. Med.*, 2008, **44**, 1120-1130.

11 J. Xu, Y. Sun, J. Huang, C. Chen, G. Liu, Y. Jiang, Y. Zhao and Z. Jiang, *Bioelectrochemistry*, 2007, **71**, 217-222.

12 N. Lagopati, P. V. Kitsiou, A. I. Kontos, P. Venieratos, E. Kotsopoulou, A. G. Kontos, D. D. Dionysiou, S. Pispas, E. C. Tsilibary and P. Falaras, *J. Photochem. Photobiol. A*, 2010, **214**, 215-223.

13 T. Lopez, E. Ortiz, M. Alvarez, J. Navarrete, J. A. Odriozola, F. Martinez-Ortega, E. A. Paez-Mozo, P. Escobar, K. A. Espinoza and I. A. Rivero*, Nanomed.-Nanotechnol. Biol. Med.*, 2010, **6**, 777-785.

14 R. Cai, Y. Kubota, T. Shuin, H. Sakai, K. Hashimoto and A. Fujishima, *Cancer Res.*, 1992, **52**, 2346-2348.

15 S. Zhang, D. Yang, D. Jing, H. Liu, L. Liu, Y. Jia, M. Gao, L. Guo and Z. Huo, *Nano Res.*, in press.

16 L. Wang, J. Shi, R. Liu, Y. Liu, J. Zhang, X. Yu, J. Gao, C. Zhang and Z. Zhang, *Nanoscale*, 2014, **6**, 4642-4651.

17 B. M. Maciejewska, A. Warowicka, A. Baranowska-Korczyc, K. Załęski, T. Zalewski, K. K. Kozioł, and S. Jurga, *Carbon*, 2015, **94**, 1012-1020.

18 K. A. Michalow, D. Flak, A. Heel, M. Parlinska-Wojtan, M. Rekas and T. Graule, *Environ. Sci. Pollut. Res.*, 2013, **19**, 3696-3708.

19 K. A. Michalow, E. H. Otal, D. Burnat, G. Fortunato, H. Emerich, D. Ferri, A. Heel and T. Graule, *Catal. Today*, 2013, **209**, 47-53.

20 C. A. Robertson, D. H. Evans and H. Abrahamse, *J. Photochem. Photobiol. B*, 2009, 96, 1-8.

21 H. Zhang, Y. Shan and L. Dong, *J. Biomed. Nanotechnol.*, 2014, **10**, 1450-1457.

22 K. H. Hu, S. H. Wang, T. Hsu, C. C. Chen, T. Y. Lin, H. T. Tsai and H. H. Chiang, *J. Nanomater.*, 2012, **2012**, 1-6.

23 M. Landmann, E. Rauls and W. G. Scmidt, *J. Phys.-Condes. Matter.*, 2012, **24**, 1-6.

24 D. H. Kim, H. S. Hong, S. J. Kim, J. S. Song and K. S. Lee, *J. Alloy. Compd.*, 2004, **375**, 259-264.

25 Y. Wang, H. Cheng, Y. Hao, J. Ma, W. Li and S. Cai, *J. Mater. Sci.*, 1999, **34**, 3721-3729.

26 L. Sang, J. L. Gole, J. Wang, J. Brauer, B. Mao, S. M. Prokes and C. Burda, J. *Phys. Chem. C*, 2013, **117**, 15287-15294.

27 K. F. Moura, J. Maul, A. R. Albuquerque, G. P. Casali, E. Longo, D. Keyson, A. G. Souza, J. R. Sambrano and I. M. G. Santos, *J. Solid State Chem.*, 2014, **210**, 171-177.

28 A. Orendorza, A. Brodyanskib, J. Löschb, L. H. Baic, Z. H. Chenc, Y. K. Lec, C. Zieglera and H. Gnaser, *Surf. Sci.*, 2007, **601**, 4390-4394.

29 A. Abidov, B. Allabergenov, J. Lee, H.-W. Jeon, S.-W. Jeong and S. Kim, Int. *J. Mater. Mech. Manuf.*, 2013, **1**, 294-296.
30 I. Iatsunskyi, M. Kempiński, G. Nowaczyk, M. Jancelewicz, M. Pavlenko, K. Załęski and S. Jurga, *Appl. Surf. Sci.*, 2015, **347**, 777-783.
31 M. C. Biesinger, B. P. Payne, A. P. Grosvenor, L. W. M. Lau, A. R. Gerson and R. S. C. Smart, *Appl. Surf. Sci.*, 2011, **257**, 2717-2730.
32 K. Plaetzer, T. Kiesslich, C. B. Oberdanner and B. Krammer, *Curr. Pharm. Design*, 2005, **11**, 1151-1165.
33 P. F. R. Palma, G. L. Baggio, C. Spada, da Silva R., S. I. A. C. P. Ferreira and A. Treitinger, *Braz. J. Infect. Dis.*, 2008, **12**, 108-114.
34 S. George, S. Pokhrel, Z. Ji, B. L. Henderson, T. Xia, L. Li, J. I. Zink, A. E. Nel and L. Maedler, *J. Am. Chem. Soc.*, 2011, **133**, 11270-11278.
35 A. R. Lupu and T. Popescu, *Toxicol. in Vitro*, 2013, **27**, 1445.
36 S. M. Chiu, L. Y. Xue, M. Lam, M. E. Rodriguez, P. Zhang, M. E. Kenney, A. L. Nieminen and N. L. Oleinick, *Photochem. Photobiol.*, 2010, **86**, 1161-1173.